

*Citation for published version:*

Scobie, JA, Sangan, CM, Owen, JM, Wilson, M & Lock, GD 2014, 'Experimental measurements of hot gas ingestion through turbine rim seals at off-design conditions', *Proceedings of the Institution of Mechanical Engineers Part A: Journal of Power and Energy*, vol. 228, no. 5, pp. 491-507.  
<https://doi.org/10.1177/0957650914527273>

*DOI:*

[10.1177/0957650914527273](https://doi.org/10.1177/0957650914527273)

*Publication date:*

2014

*Document Version*

Early version, also known as pre-print

[Link to publication](#)

## University of Bath

### Alternative formats

If you require this document in an alternative format, please contact:  
[openaccess@bath.ac.uk](mailto:openaccess@bath.ac.uk)

#### General rights

Copyright and moral rights for the publications made accessible in the public portal are retained by the authors and/or other copyright owners and it is a condition of accessing publications that users recognise and abide by the legal requirements associated with these rights.

#### Take down policy

If you believe that this document breaches copyright please contact us providing details, and we will remove access to the work immediately and investigate your claim.

# **Experimental measurements of hot gas ingestion through turbine rim seals at off-design conditions**

**James A Scobie, Carl M Sangan, J Michael Owen, Michael Wilson and Gary D Lock**

Department of Mechanical Engineering, University of Bath, Bath, UK

## **Abstract**

This paper describes results obtained from an experimental facility which models ingress through the rim seal into the upstream wheel-space of an axial-turbine stage. The experimental rig included 32 nozzle guide vanes and 41 symmetrical turbine blades, and the paper presents measurements of  $\varepsilon$  (the sealing effectiveness) for single- and double-clearance seals for both over-speed (where the blades rotate faster than at the design point) and under-speed conditions. The design flow coefficient was  $C_F = 0.538$ , and tests were conducted for  $0 < C_F < 0.9$ , which is larger than the range experienced in engines. The measured values of  $\varepsilon$  were correlated by the ‘effectiveness equations’ for rotationally-induced (RI) and externally-induced (EI) ingress.

The correlated effectiveness curves were used to determine  $\Phi_{min}'$  (the value of the sealing flow parameter when  $\varepsilon = 0.95$ ), and the variation of  $\Phi_{min}'$  with  $C_F$  was in mainly good agreement with the theoretical curve for CI (combined ingress), which covered the transition from RI to EI ingress. Departure of the measured values of  $\Phi_{min}'$  from the CI curve occurred at very low values of  $C_F$  for all the seals tested; this was attributed to the effects of separation of the mainstream flow over the turbine blades at large ‘deviation angles’ between the flow and the blades.

The measurements are expected to be qualitatively similar to but quantitatively different from those experienced in engines.

## Keywords

Gas turbines, air cooling, industrial turbomachinery

## Introduction

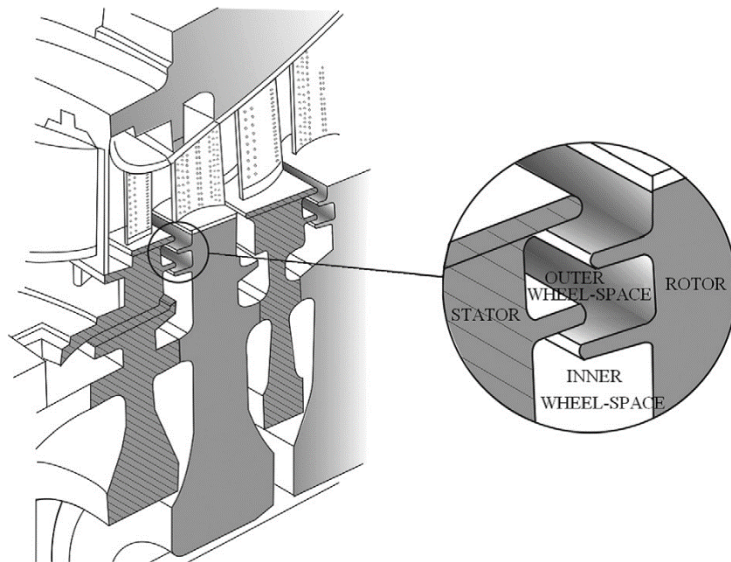


**Figure 1.** Typical high-pressure gas-turbine stage and detail of rim seal

The rim seal of a gas turbine (see Figure 1) reduces the amount of hot gas ingestion (referred to below as *ingress*) into the turbine wheel-space radially-inward of the seal. Sealing air, produced by the compressor, is supplied to pressurise the wheel-space. Although essential, this sealing air reduces the engine performance in two ways: much of the power taken to compress the air is dissipated; the *egress*, or air leaving the seal, mixes with the mainstream gas flow and creates aerodynamic losses. The designer needs

to optimise the amount of sealing air used: too much creates extra losses; too little could cause overheating of the turbine disc and blade roots, resulting in catastrophic failure.

The flow past the stationary vanes and rotating blades in the turbine annulus creates an unsteady 3D variation of pressure radially outward of the rim seal. The magnitude of this pressure asymmetry at the seal clearance depends on the location of the clearance relative to the vanes and blades. Ingress and egress occur through those parts of the seal clearance where the external pressure is higher and lower, respectively, than that in the wheel-space; this non-axisymmetric type of ingestion is referred to here as *externally-induced (EI) ingress*.

Even if the external flow were axisymmetric, with no circumferential variation of external pressure, ingress would still occur. The reason for this is that the rotating fluid in the wheel-space creates a radial gradient of pressure, so that the pressure inside the wheel-space can drop below that outside. The so-called ‘disc-pumping effect’ causes the egress of fluid near the rotating disc, and the low pressure in the wheel-space causes ingress of external fluid through the rim seal into the wheel-space. This type of ingestion is referred to here as *rotationally-induced (RI) ingress*.

All gas turbines spend some time (e.g. during starting, idling, reduced power, maximum power, acceleration and deceleration) at off-design conditions far removed from the design point of the turbine. Satisfactory off-design operation over a wide range of rotational speeds and inlet conditions is therefore an important requirement for all engines. In the case where the rotational speed of the engine is constant, such as in a single-shaft industrial turbine, performance can be improved by actively controlling the flow rate through the compressor using variable vanes. These vanes change the design point of the compressor but not that of the turbine, and the off-design operation of the turbine may have a significant effect on ingestion.

The flow in the mainstream annulus of the turbine is usually characterised by the flow coefficient,  $C_F$ . (In many textbooks and papers, the symbol  $\phi$  is used to denote the flow coefficient. As this symbol could

be confused with the angular coordinate in the cylindrical-polar coordinates used by the authors, the symbol  $C_F$  is used in this paper.) The definition of  $C_F$  used here is

$$C_F = \frac{W}{\Omega b} \quad (1)$$

where  $W$  is the mean axial component of velocity in the annulus downstream of the turbine vanes,  $b$  is the outer radius of the turbine disc and  $\Omega$  is its angular speed. For a given exit angle of the vanes,  $C_F$  defines the swirl ratio of the mainstream flow, and at the design point of engines  $C_F \approx 0.5$ . Modern turbines, with larger vane exit-angles, tend to operate at lower values of  $C_F$  than the older ones.

The pressure asymmetry in the annulus, and consequently EI ingress, increases as  $C_F$  increases. At the design point, where rotational effects are relatively small, EI ingress is usually assumed to dominate. However, at over-speed or low- $C_F$  conditions rotation can have a significant effect on ingress, and the term *combined ingress (CI)* is used here to denote the ingestion that occurs when the effects of rotation and the external-pressure distribution are both significant. For off-design operation, it is important to consider combined ingress as the general case with EI and RI ingress as special or limiting cases.

The authors<sup>1-9</sup> have successfully used orifice models to determine the sealing effectiveness of a wide range of seal geometries. In previous publications<sup>7-9</sup>, solutions of the so-called RI and EI effectiveness equations, derived from the orifice models, have been compared with concentration measurements made at the design point of a single-stage turbine rig. In this paper, solutions of the equations for CI, EI and RI ingress are compared with effectiveness measurements made at off-design conditions.

The following section presents a brief review of the relevant research. The details of the experimental apparatus used for the effectiveness measurements in this study are then described. Next, the measurements of pressure in the annulus are presented, and then the sealing effectiveness, and comparisons with the

solutions of the orifice models, is discussed. Finally, the main conclusions are summarised, and the relevant equations derived from the orifice models for CI, EI and RI ingress are given in Appendix 2.

## **Review of relevant papers**

At the design point in a gas turbine, ingestion of hot gas through the rim seal is dominated by EI ingress. However, at off-design conditions, the effects of rotation can be significant. These conditions lead to combined ingress (CI) involving both externally-induced (EI) and rotationally-induced (RI) ingress. Consequently, this brief review is principally concerned with experimental papers on combined ingress, and the reader is referred to the preceding Bath papers<sup>1-9</sup> if more details of the ingress problem are required.

Phadke and Owen<sup>10,11</sup> correlated  $C_{w,min}$ , the minimum sealing flow rate needed to prevent ingress, in a simple rotor-stator system with a number of different rim-seal geometries. Their tests were conducted without vanes and blades in the external annulus, and circumferential pressure asymmetries were created by blocking sections of the annulus with honeycomb and wire mesh. The tests showed that EI ingress was caused by the pressure asymmetry produced by the external flow. For  $Re_w = 0$ , where RI ingress occurs,  $C_{w,min} \propto Re_\phi$ ; for large values of  $Re_w$ , where EI ingress dominates,  $C_{w,min} \propto Re_w$ . The term combined ingress is now used to denote the transition from RI to EI ingress.

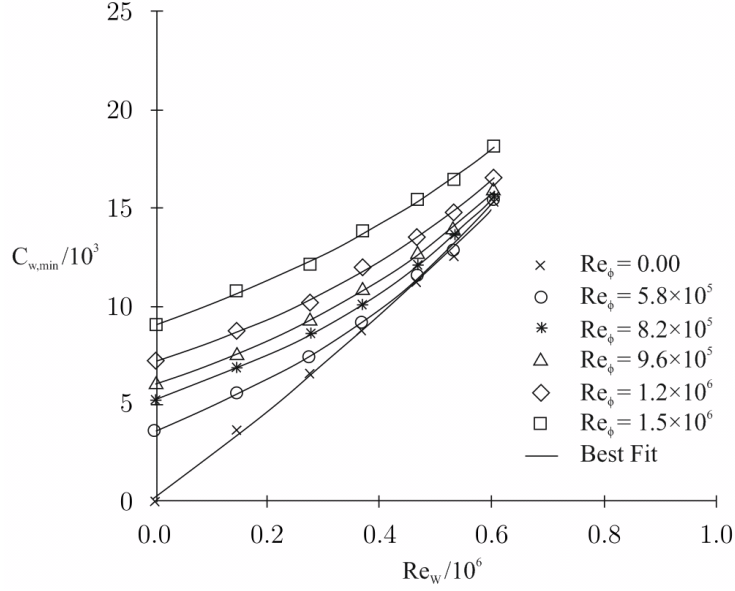


**Figure 2.** Effect of  $Re_\phi$  on variation of  $C_{w,min}$  with  $Re_w$  (Khilnani and Bhavnani<sup>12</sup>)

Khilnani and Bhavnani<sup>12</sup> investigated the sealing performance of an axial seal in a rig without blades or vanes. Eccentricity in the external annulus caused circumferential variations in the external pressure, and static pressure measurements in the wheel-space were used to determine  $C_{w,min}$  for a range of  $Re_w$  and  $Re_\phi$ . Figure 2 shows the effect of  $Re_\phi$  on the variation of  $C_{w,min}$  with  $Re_w$ , and their results were broadly consistent with those of Phadke and Owen.

Owen et al.<sup>4</sup> fitted the CI equation developed from their orifice model (see Owen<sup>2</sup>) to the experimental data of Phadke and Owen<sup>11</sup>. The CI equation (see Appendix 2) can be written as

$$\frac{\Phi_{min,CI}}{\Phi_{min,RI}} = \frac{2}{3} \frac{\left[1 + k_c (W/\Omega b)^2\right]^{3/2} - 1}{k_c (W/\Omega b)^2} \quad (2)$$

where  $k_c$  is an empirical constant and the other symbols are defined in the Nomenclature. Now, as

$$\frac{\Phi_{\min,CI}}{\Phi_{\min,RI}} = \frac{C_{w,\min,CI}}{C_{w,\min,RI}} \quad (3)$$

and

$$\frac{W}{\Omega b} = \frac{Re_w}{Re_\phi} \quad (4)$$

equation (2) can be written as

$$\frac{C_{w,\min,CI}}{C_{w,\min,RI}} = \frac{2}{3} \frac{\left[1 + k_c (Re_w/Re_\phi)^2\right]^{3/2} - 1}{k_c (Re_w/Re_\phi)^2} \quad (5)$$

The RHS of equation (5) approaches the EI asymptote as  $Re_w/Re_\phi \rightarrow \infty$ , and equation (5) becomes

$$\frac{C_{w,\min,CI}}{C_{w,\min,RI}} = \frac{2}{3} k_c^{1/2} \frac{Re_w}{Re_\phi} \quad (6)$$

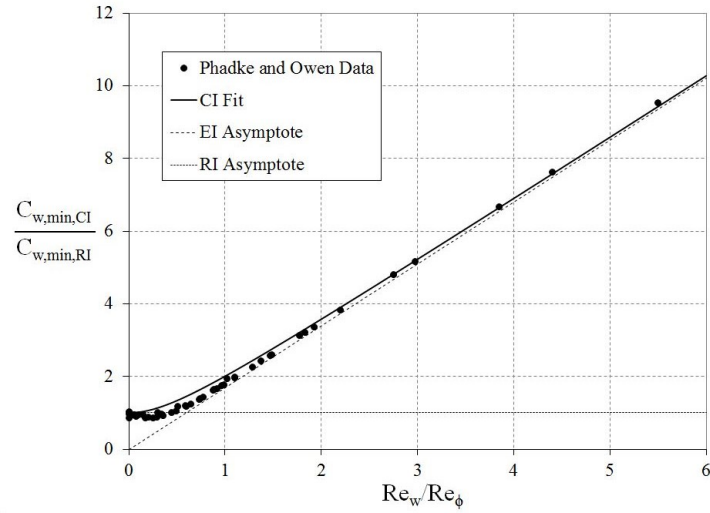


**Figure 3.** CI equation fitted to data of Phadke and Owen<sup>11</sup>.

Solid line is equation (5); broken line is equation (6)



The CI equation (5) is shown fitted to the data of Phadke and Owen<sup>11</sup> in Figure 3 and to the data of Khilnani and Bhavnani<sup>12</sup> in Figure 4. (The data shown in Figure 4 were obtained from the data shown in Figure 2; Figure 4 was not shown in the paper of Khilnani and Bhavnani<sup>12</sup>.) In both figures, the CI equation captures the transition from RI to EI ingress and collapses the data obtained for a wide range of  $Re_w$  and  $Re_\phi$  onto a single curve. The fact that the  $C_{w,min}$  ratio in Figure 4 is much higher than that in Figure 3 is attributed to the fact that the pressure asymmetry in the annulus of the rig of Khilnani and Bhavnani was significantly higher than that in the rig of Phadke and Owen. It should also be noted that the departure of the CI curve from its EI asymptote increases as  $Re_w/Re_\phi$  decreases.

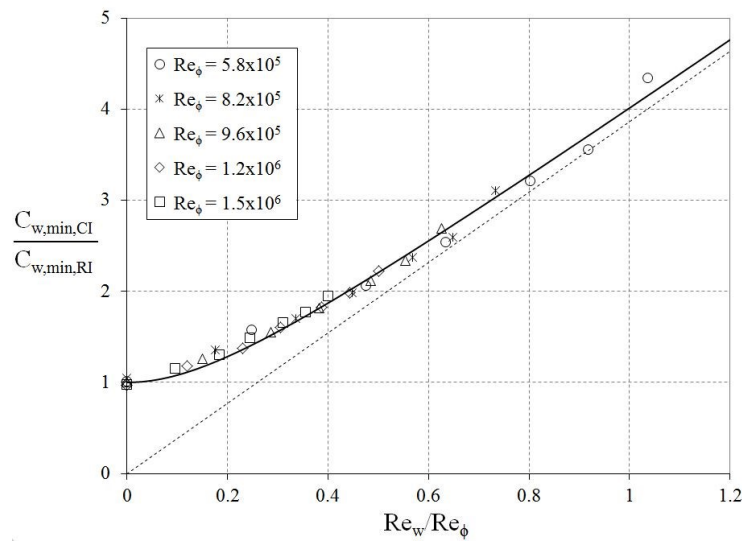


**Figure 4.** CI equation fitted to data of Khilnani and Bhavnani<sup>12</sup>.

Solid line is equation (5); broken line is equation (6)

Although the CI equation gives a good fit to the data in the above cases, there were no vanes or blades in the annuli of the experimental rigs. By contrast, Green and Turner<sup>13</sup> made concentration measurements in a rig that incorporated both vanes and blades, with the axial-seal clearance located close to the leading edge of the blades. The authors unexpectedly showed that the effect of blades on the rotor was to *reduce*

ingestion rather than increase it. However this finding was later questioned by Hills et al.<sup>14</sup> who highlighted uncertainty in the “vanes-only” measurements in Green and Turner’s work. Hills et al. themselves concluded through CFD calculations that unsteadiness due to the rotor blade will usually lead to *more* ingestion.

Experiments conducted by Bohn et al.<sup>15</sup> with a shrouded stator and unshrouded rotor showed an increase in sealing efficiency when blades were introduced; the opposite effect was shown for the case with two unshrouded discs. Unsteady LDV measurements made by Bohn et al.<sup>16</sup> in a 1.5 stage turbine rig then showed ingestion intensified as the rotor blades passed through the stator wake.

The conflicting results found in these studies highlight that the effect of rotor blades on ingress is complex. As noted by Gentilhomme et al.<sup>17</sup>, the amount of ingress will depend on the vane, blade and seal geometries, as well as the relative location of the seal clearance.

There is a growing trend in industry to use complex 3D unsteady CFD codes to explore the mechanisms of ingress, such as O’Mahoney et al.<sup>18</sup>. However there is also a requirement for detailed measurements in simplified engine rigs specifically designed for instrumentation access to validate these codes.

## **Experimental procedure**

### *Experimental Facility*

The research facility, which experimentally simulates hot gas ingress into the wheel space of an axial turbine stage, is described extensively in Sangan et al.<sup>7</sup> The test section of the facility, shown in Figure 5, features a turbine stage with 32 vanes and 41 blades, which were formed from nylon by rapid-prototyping. The disc and blades were rotated by an electric motor. The blades were symmetric NACA 0018 aerofoils to avoid the necessity of a dynamometer to remove the unwanted power; the ratio of the leading-edge

diameter to chord-length was 0.0984. The diameter of the disc was 380 mm and the height of the annulus was 10 mm.

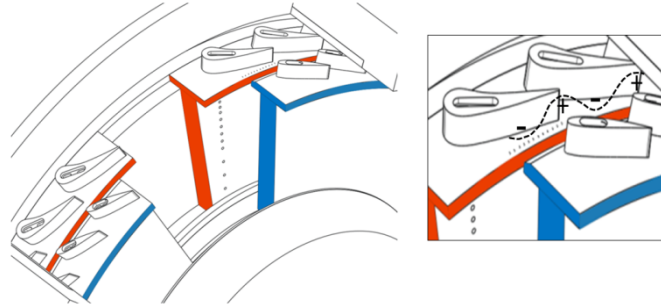


**Figure 5.** Rig test section with inset highlighting the static pressure taps in the vane hub (location A) and typical pressure asymmetry in the annulus. (Red indicates the stationary disc and blue the rotating disc)

The disc could be rotated up to speeds of 4000 rpm, providing a maximum rotational Reynolds numbers,  $Re_\phi$  (based on disc radius) up to  $1.1 \times 10^6$ . This value is typically an order-of-magnitude less than that found in gas turbines. However, for rotating flow the turbulent flow structure in the boundary layers is principally governed by the turbulent flow parameter  $\lambda_T$  and depends only weakly on  $Re_\phi$  (Owen and Rogers<sup>19</sup>). Hence, the flow structure in the rig is considered to be representative of that found in the cooling systems of engines.

The vanes and blades in the annulus also produced a flow structure representative of those found in engines, albeit at lower Reynolds and Mach numbers. The circumferential variation of static pressure was determined from 15 taps (each 0.5 mm diameter) arranged across one vane pitch, as illustrated in Figure 5 (inset); these taps were located in the vane platform 2.5 mm downstream of the vane trailing edge (location A) and in the outer casing above the centre-line of the seal clearance (location B). Data was averaged over four vane pitches. The pressures were measured using a Scanivalve system, which was connected to the taps with flexible plastic tubing.

Sealing air was introduced into the wheel-space at a low radius ( $r/b = 0.642$ ) through an inlet seal. To measure the degree of ingestion, the sealing flow was seeded with a carbon dioxide tracer gas. The concentration of  $\text{CO}_2$  was monitored at the entrance to the wheel-space  $c_0$  and in the unseeded upstream flow through the annulus  $c_a$ . The concentration in the wheel-space,  $c_s$ , was measured on the stator wall at locations  $r/b = 0.958$  and  $0.850$  and was determined by sampling through hypodermic tubes of diameter 1.6 mm. The gas was extracted by a pump, which delivered the samples to an infrared gas analyzer.

Concentration measurements were used to determine the *concentration effectiveness*  $\varepsilon_c$ . This is defined as

$$\varepsilon_c = \frac{c_s - c_a}{c_0 - c_a} \quad (7)$$

where the subscripts  $a$ ,  $0$  and  $s$  respectively denote the air in the annulus, the sealing air at inlet, and at the surface of the stator. In particular,  $\varepsilon_c = 1$  when  $c_s = c_0$  (zero ingress) and  $\varepsilon_c = 0$  when  $c_s = c_a$  (zero sealing flow).

All data presented in this paper are for three rotational disc speeds (corresponding to  $Re_\phi = 5.32 \times 10^5$ ,  $8.17 \times 10^5$  and  $9.68 \times 10^5$ ), with the mainstream flow-rate varied to create the *off-design* velocity triangles in the turbine annulus. On design  $Re_w/Re_\phi = 0.538$ , where  $Re_w$  is the Reynolds number based on the axial component of velocity in the annulus. Off-design  $Re_w/Re_\phi$  (which is analogous to the flow coefficient,  $C_F$ —see Appendix 2) is varied from zero (i.e. in the absence of external flow) up to 0.858. When  $C_F < 0.538$ , the rig was operating at an over-speed condition; when  $C_F > 0.538$ , the rig was operating at an under-speed condition.

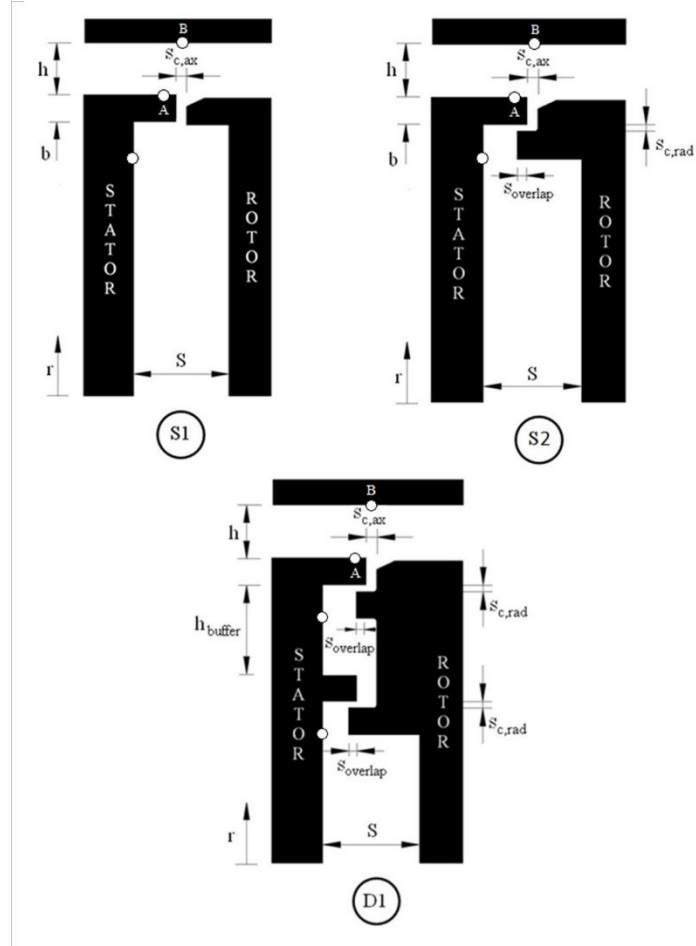


**Figure 6.** Rim-seal configurations

### *Details of Rim-Seal Configurations*

Two single seal configurations and a double-clearance configuration were investigated: an axial-clearance seal (S1), a radial clearance seal (S2) and a double radial seal (D1). Schematics of the seal geometries are shown as Figure 6 and static dimensions are given Table 1. The simple axial-clearance seal (S1) is formed between the vane and blade platforms which co-exist at the wheel-space periphery. The radial-clearance seal (S2) features an identical geometry at the wheel-space periphery, with an axial-overlap

from a radial lip at lower radius on the rotor. A secondary inner radial-clearance seal was further added to seal configuration S2, to produce double seal, D1. For this configuration, an outer seal was formed at the periphery of the wheel-space and a secondary inner seal was located radially inward at  $r/b = 0.88$ .

The seal-clearance ratio,  $G_c = s_{c,ax} / b = 0.0105$  used in equation (16) for all seal geometries, is based on the axial clearance  $s_{c,ax} = 2.0$  mm.

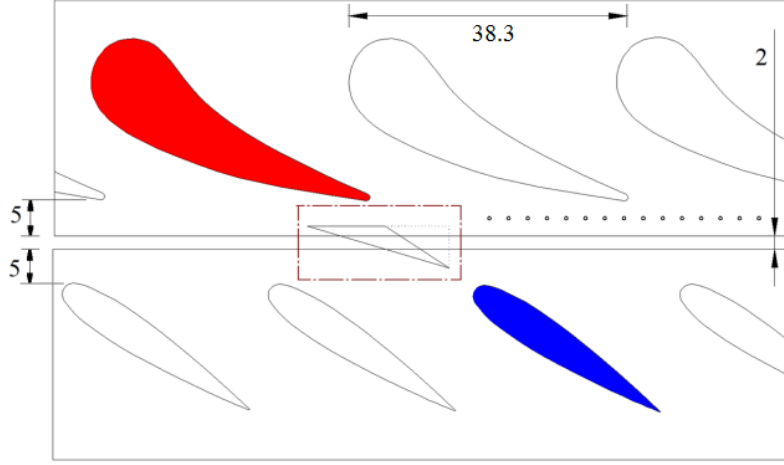
Geometric Symbol	Seal Configuration		
	S1	S2	D1
h	10.0		
b	190		
S	20.0		
$s_{c,ax}$	2.00		
$s_{c,rad}$	-	1.28	1.28
Soverlap	-	1.86	1.86
$h_{buffer}$	-	-	16.5

**Table 1.** Geometric properties for all seal configurations (dimensions in mm under static conditions)

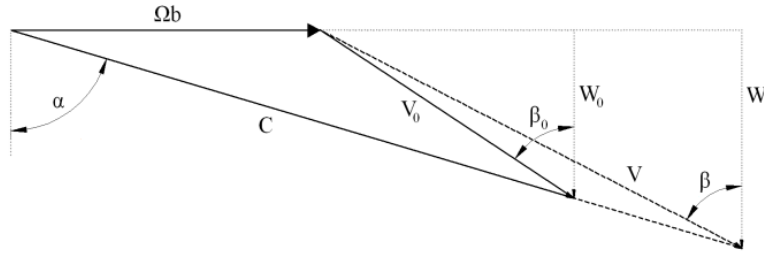
## Pressure Measurements

### *Flow Direction Relative to the Blade*

Figure 7 shows the profiles and velocity triangles for the vanes and the symmetrical blades, where  $\alpha$  and  $\beta$  are the respective angles of the resultant velocity of the flow, relative to the axial direction, in the stationary and rotating frames. In the rig,  $\alpha$  is  $73^\circ$  and  $\beta_0$ , the blade angle, is  $56^\circ$ ; at the design condition,  $\beta = \beta_0$ ; at off-design conditions,  $\beta - \beta_0$  is the ‘deviation angle’ between the resultant velocity in the rotating frame and the blade.



(a) Profiles of vanes and blades



(b) Velocity triangles

**Figure 7.** Profiles and velocity triangles for vanes and blades

( $\beta - \beta_0$  is the ‘deviation angle’ between the resultant velocity in the rotating frame and the blade.)

From the velocity triangles, it follows that

$$\tan \beta = \tan \alpha - \left( \frac{W}{\Omega b} \right)^{-1} = \tan \alpha - C_F^{-1} \quad (8)$$

where  $C_F = W/\Omega b$  is the flow coefficient. At the design point, which is denoted by the subscript  $0$ ,

$$\tan \beta_0 = \tan \alpha - \left( \frac{W}{\Omega b} \right)_0^{-1} = \tan \alpha - C_{F,0}^{-1} \quad (9)$$

and, the flow coefficient at the design point for the rig was  $C_{F,0} = 0.538$ . For the *over-speed condition*, where  $C_F < 0.538$ ,  $\beta < \beta_0$ ; for the *under-speed condition*,  $\beta > \beta_0$ . When  $\Omega = 0$  or  $W \rightarrow \infty$ ,  $\beta = \alpha$  and  $\beta - \beta_0 = 17^\circ$ ; when  $W = 0$ ,  $\beta = -\pi/2$  and  $\beta - \beta_0 = -146^\circ$ .

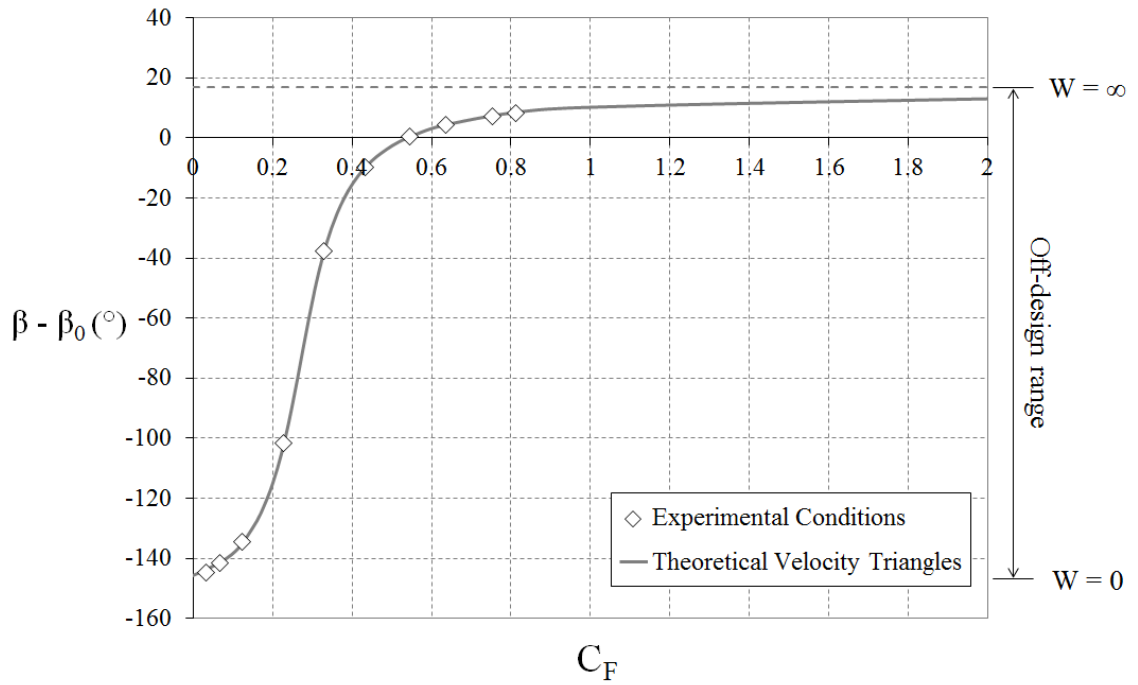


**Figure 8.** Variation of deviation angle with flow coefficient

(Symbols denote where concentration measurements were made for axial-clearance seal.)

Figure 8 shows the variation of the deviation angle,  $\beta - \beta_0$ , with the flow coefficient, and the symbols denote where measurements were made for the axial-clearance seal. The experimental range exceeded any range likely to be experienced in an engine, particularly at the low values of  $C_F$ .



### Pressure measurements in the annulus

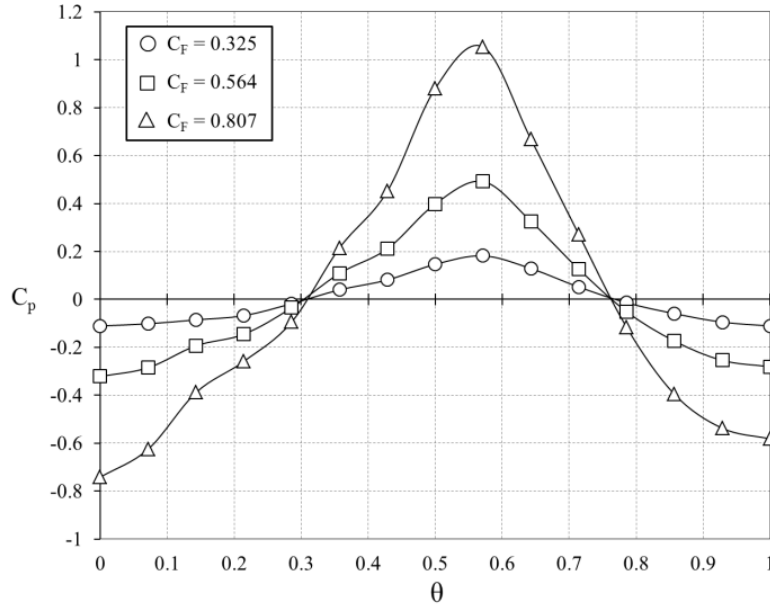


**Figure 9.** Effect of flow coefficient on circumferential distribution of  $C_p$  measured at location A over one vane pitch in the absence of sealing flow

Figure 9 shows the effect of  $C_F$  on the circumferential distribution of  $C_p$  where

$$C_p = \frac{p - \bar{p}}{\frac{1}{2} \rho \Omega^2 b^2} \quad (10)$$

The static pressures were measured on the vane platform downstream of the vanes in the absence of sealing flow, and  $\bar{p}$  is the mean static pressure over one vane pitch.

According to the orifice model, details of which are summarised in Appendix 2, EI ingress is related to the nondimensional pressure difference in the annulus,  $\Delta C_p$ , where

$$\Delta C_p = \frac{\Delta p}{\frac{1}{2}\rho \Omega^2 b^2} \quad (11)$$

$\Delta p$  being the peak-to-trough static-pressure difference.  $\Delta C_p$ , which is equivalent to the peak-to-trough difference of  $C_p$ , increases as flow coefficient increases.

As shown by equation (18), the sealing parameter necessary to prevent EI ingress,  $\Phi_{min,EI}$ , is related to  $\Delta C_p$  by

$$\Phi_{min,EI} = \frac{2}{3} C_{d,e} \Delta C_p^{1/2} \quad (12)$$

where  $C_{d,e}$  is the discharge coefficient for egress through the rim seal. Sangan et al.<sup>7</sup> showed that  $\Delta C_p$  decreases slightly as the flow rate of sealing air increases.

For mathematical consistency in the EI orifice model, it is necessary that there is zero ingress when  $\Delta C_p = 0$ . However, as shown below, the value of  $\Delta C_p$  depends on where in the annulus it is evaluated. (As shown in Sangan et al.<sup>7</sup>, the consistency criterion can only be satisfied in small regions near the rim seal, and the values of  $\Delta C_p$  measured in an experimental rig are unlikely to satisfy this criterion.)

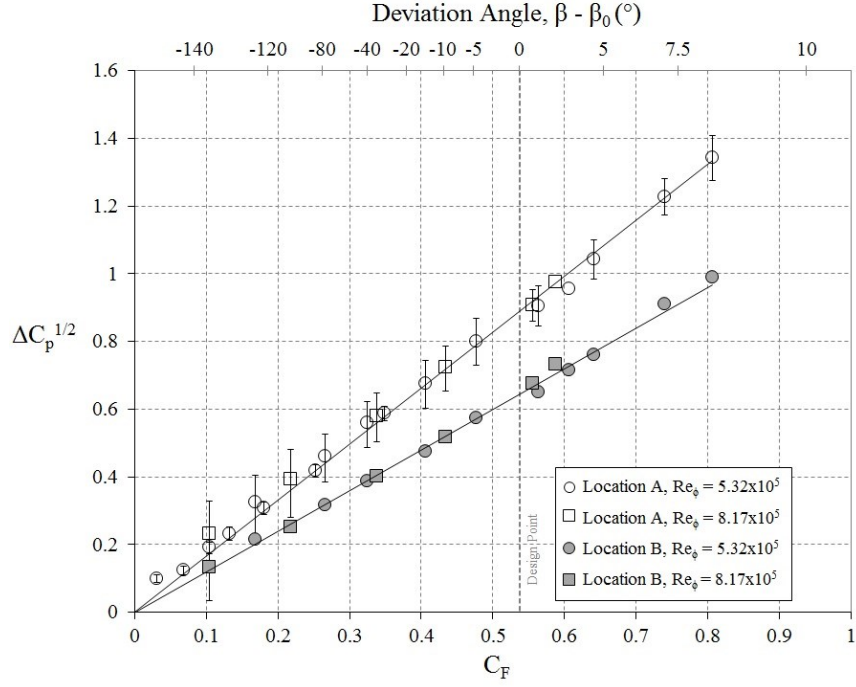


**Figure 10.** Measured variation of  $\Delta C_p^{1/2}$  at locations A and B in annulus with flow coefficient and with deviation angle

Figure 10 shows the measured variation of  $\Delta C_p^{1/2}$  with the flow coefficient, and with the deviation angle  $\beta - \beta_0$ , measured at locations A and B in the annulus. The experimental measurements show no significant effect of  $Re_\phi$ , and  $\Delta C_p^{1/2}$  increases linearly with  $C_F$ ; despite the large experimental range, there is no obvious effect of the deviation angle on this linear variation.

The experimental data in Figure 10 for location A were correlated by

$$\Delta C_p^{1/2} = k_a C_F \quad (13)$$

where  $k_a = 1.66$

## Concentration Measurements

Results for two single and one double seal are presented here, principally to illustrate the similarities between the off-design performance of different seals. There are, of course, quantitative differences in the effectiveness of these seals, and the reader is referred to previous publications<sup>7-9</sup> if more details of their relative performance are required.

### *Variation of Sealing Effectiveness*

For the single seals, and for the outer seal in the double-seal tests, the effectiveness values were based on the concentration measurements at  $r/b = 0.958$ ; for the inner seal in the double-seal tests, the location was  $r/b = 0.85$ . The data were fitted using the effectiveness equations given in Appendix 2, and the values of  $\Phi_{min}$  and  $\Gamma_c$  were found using the statistical technique described in Zhou et al.<sup>5</sup>. For  $C_F = 0$ , the RI effectiveness equation (21), was used; for  $C_F > 0$ , the EI equation (17), was used. Although effectiveness measurements were made for many values of the flow coefficient, the results of only four cases are shown below. These correspond to  $C_F = 0$ , and to values of  $C_F$  for the over-speed, design and under-speed conditions. As they showed nothing of particular interest, the effectiveness curves for the double seal are not shown here.

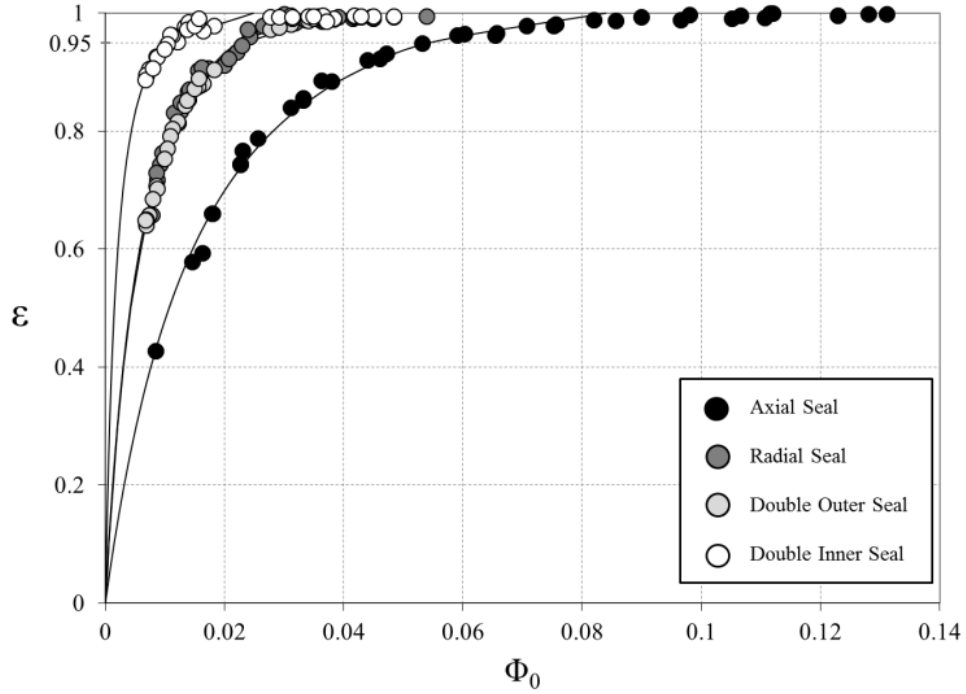


**Figure 11.** Variation of sealing effectiveness with  $\Phi_0$  for RI ingress for four seals  
Symbols denote experimental data; lines are theoretical curves.

Figure 11 shows the variation of  $\varepsilon$  with  $\Phi_0$  for the case where the external flow was zero, which (as shown in Sangan et al.<sup>8</sup>) corresponds to RI ingress. The RI effectiveness equation (21) was fitted to the experimental data using the statistical technique described in Zhou et al.<sup>5</sup>, and the agreement between the theoretical curve and the data is very good for all the seals shown in Figure 6. It can be seen that the results for the outer seal of the double-seal (D1 outer) agree very closely with those for the single radial seal (S2), and the radial-clearance seal is much more effective than the axial-clearance one (S1).

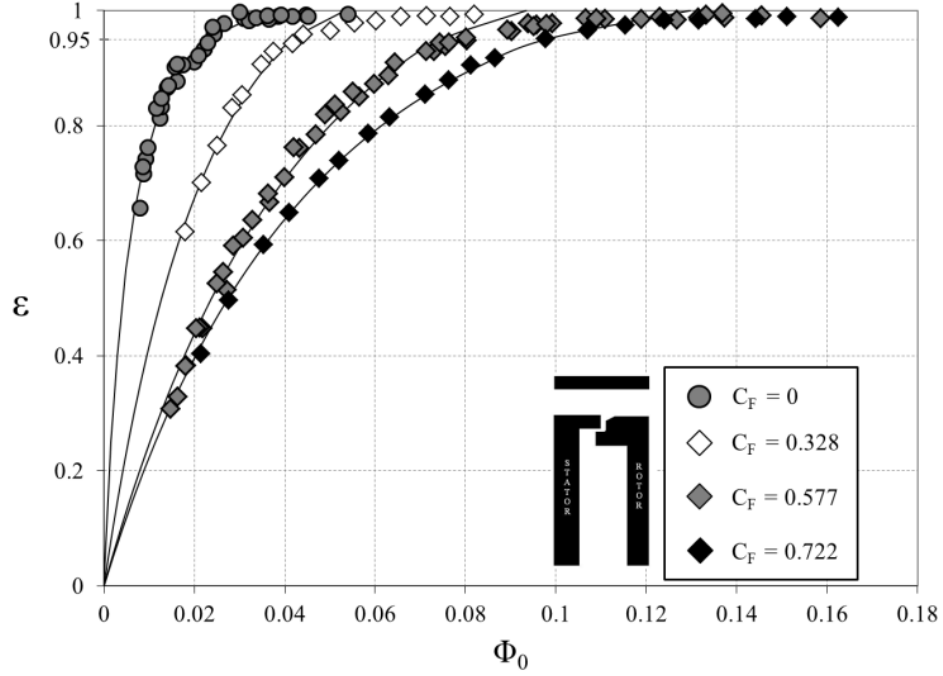


**Figure 12.** Effect of flow coefficient on variation of effectiveness with sealing parameter for radial-clearance seal

Symbols denote experimental data; lines are theoretical curves

Figure 12 shows the effect of the flow coefficient on the variation of the sealing effectiveness with the sealing parameter,  $\Phi_0$ , for the radial-clearance seal (S2 in Figure 6). The effectiveness decreases as  $C_F$  increases, which is consistent with the pressure measurements discussed above where  $\Delta C_p$  increases as  $C_F$  increases. In some of the experiments it proved impossible to achieve a fully sealed system but, apart from the values near  $\varepsilon = 1$ , the theoretical curves (with equation (17) used for  $C_F > 0$  and equation (21) for  $C_F = 0$ ) provide a good fit to the data.

Noting the different scale from that in Figure 12, Figure 13 shows the effect of  $C_F$  on the variation of  $\varepsilon$  with  $\Phi_0$  for the axial-clearance seal. For any value of  $\varepsilon$ , the values of  $\Phi_0$  are significantly larger than those for the radial-clearance seal, which is consistent with previously published measurements at the design

condition. Although there is good agreement between the theoretical curves and the data for the three smaller values of  $C_F$ , the effectiveness data for the largest value display a distinct kink around  $\Phi_0 \approx 0.2$ . If the anomalous data are removed, the remaining data can be satisfactorily fitted, as shown by the broken curve in Figure 13.

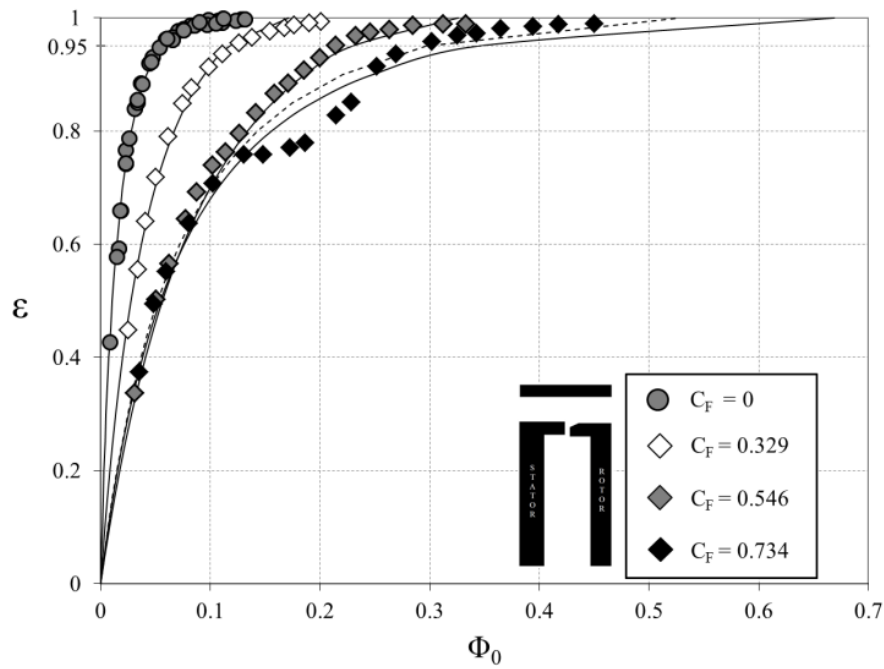


**Figure 13.** Effect of flow coefficient on variation of effectiveness with sealing parameter for axial clearance seal

Symbols denote experimental data; lines are theoretical curves

The ‘kink phenomenon’ for the axial-clearance seal was also observed at the other under-speed conditions, which are not shown here. (The phenomenon was not observed for the other three seals, for which the sealing flow rates were significantly lower.) Tests were conducted with increasing and decreasing values of  $\Phi_0$  but the results were repeatable and no hysteresis effects were found. Although pressure measurements in the annulus shed no light on the kink phenomenon, it is speculated that it might be peculiar

to the rig geometry and it could have been caused by the interaction between the sealing and mainstream flows at large sealing flow rates. Future CFD research may be able to explain this behaviour. Interestingly, Gentilhomme et al.<sup>17</sup> observed similar behaviour in their effectiveness measurement curves.

For each of the four seals tested, the values of  $\Phi_{min}$  and their confidence intervals determined from the fitted effectiveness curves could be used to produce the variation of  $\Phi_{min}$  with  $C_F$ . Before the above effectiveness curves were obtained, a separate series of concentration tests was conducted to determine  $\Phi_{min}$  for the axial-clearance seal. As it was difficult, and sometimes impossible, to determine the precise value of  $\Phi_0$  when  $\varepsilon = 1$ , the value of  $\Phi_0$  when  $\varepsilon = 0.95$  was used to define a new sealing parameter  $\Phi_{min}'$ . The measured variation of  $\Phi_{min}'$  with flow coefficient is discussed below.

#### *Variation of $\Phi_{min}'$ with Flow Coefficient*

Figure 14 shows the variation of  $\Phi_{min}'$  with flow coefficient for the axial-clearance seal where, as stated above,  $\Phi_{min}'$  denotes the value of  $\Phi_0$  when  $\varepsilon = 0.95$ . The direct measurements were of  $\Phi_{min}'$  based on concentration measurements, at  $r/b = 0.958$ , for  $Re_\phi = 5.52, 8.17$  and  $9.68 \times 10^5$ . The indirect values were calculated from the effectiveness curves discussed above, and the ‘uncertainty bars’ on the figure were based on the upper and lower bounds of the fitted effectiveness curves at  $\varepsilon = 0.95$ . (It should be noted that, at large flow coefficients where there was a kink in the effectiveness data, the effectiveness curves excluding the kinks were used to determine  $\Phi_{min}'$ .)



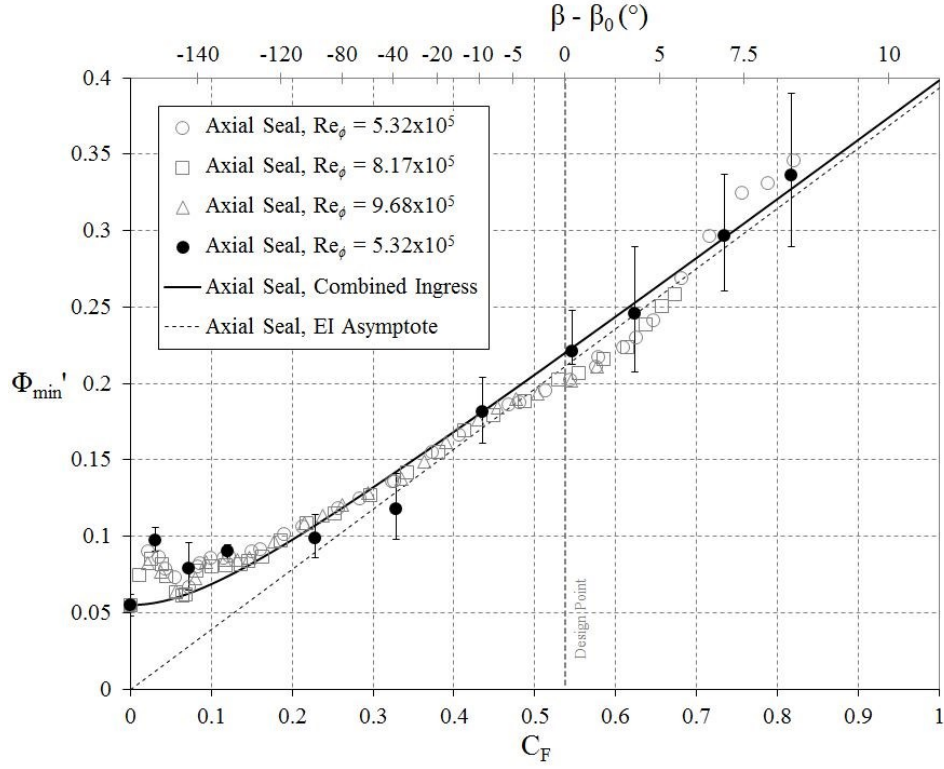


**Figure 14.** Variation of  $\Phi_{min}'$  with flow coefficient for axial-clearance seal

Solid symbols denote indirect values of  $\Phi_{min}'$  deduced from effectiveness curves; open symbols denote direct measurements of  $\Phi_{min}'$ ; solid line is fitted CI curve; broken line is EI asymptote

The fitted CI curve was obtained from equation (29) of the Appendix 2, which is rewritten here in terms of  $\Phi_{min}'$  as

$$\frac{\Phi_{min}'}{\Phi_{min,RI}'} = \frac{2}{3} \frac{[1 + k_c C_F^2]^{3/2} - 1}{k_c C_F^2} \quad (14)$$

where the constant  $k_c$  was found from a least-squares fit of the indirect measurements. (Note: the redundant subscript CI has been omitted.) For consistency with the other seals (where only indirect measurements

were made), no direct measurements were used in the fit. As  $C_F \rightarrow \infty$  and  $\Phi_{min}' \rightarrow \Phi_{min,EI}'$ , equation (14) reduces to

$$\frac{\Phi_{min,EI}'}{\Phi_{min,RI}'} = \frac{2}{3} k_c^{1/2} C_F \quad (15)$$

which is the equation for the EI asymptote shown in Figure 14. For the axial-clearance seal,  $\Phi_{min,RI}' = 0.055$  and  $k_c = 115$ ; these values and those for the other seals are shown in Table 2. As discussed previously, owing to the increasing effect of rotation the difference between the EI asymptote and the CI curve increases as  $C_F$  decreases.

Figure 14 has a similar form to Figures 3 and 4, which show the CI curve fitted to the data of Phadke and Owen (Figure 3) and Khilnani and Bhavnani (Figure 4). Unlike the rig used here, there were no vanes or blades in the external annuli of the rigs used by these two pairs of researchers; the circumferential external pressure variations in their two rigs were caused by eccentricities or partial blockages in the annuli. As noted for Figures 3 and 4, the deviation between the CI curve and the EI asymptote in Figure 14 increases as  $C_F$  decreases and as the effects of rotation increase. It can be seen that even at the design point ( $C_F = 0.538$ ) there is a small difference between the CI curve and the EI asymptote.

There appears to be no systematic departure between the measured values and the CI curve in Figure 14 until  $C_F < 0.1$ . The sudden increase in  $\Phi_{min}'$ , which is shown by the direct and indirect measurements of  $\Phi_{min}'$  at these small values of  $C_F$ , is thought to be caused by massive separation of the flow over the blades at extreme deviation angles ( $|\beta - \beta_0| > 130^\circ$ ). Although many additional measurements were conducted to confirm that this ‘blade effect’ (which also occurred for the other seals tested) was repeatable, it surprised the authors that the deviation angle appears to have no significant effect for  $|\beta - \beta_0| < 130^\circ$ .

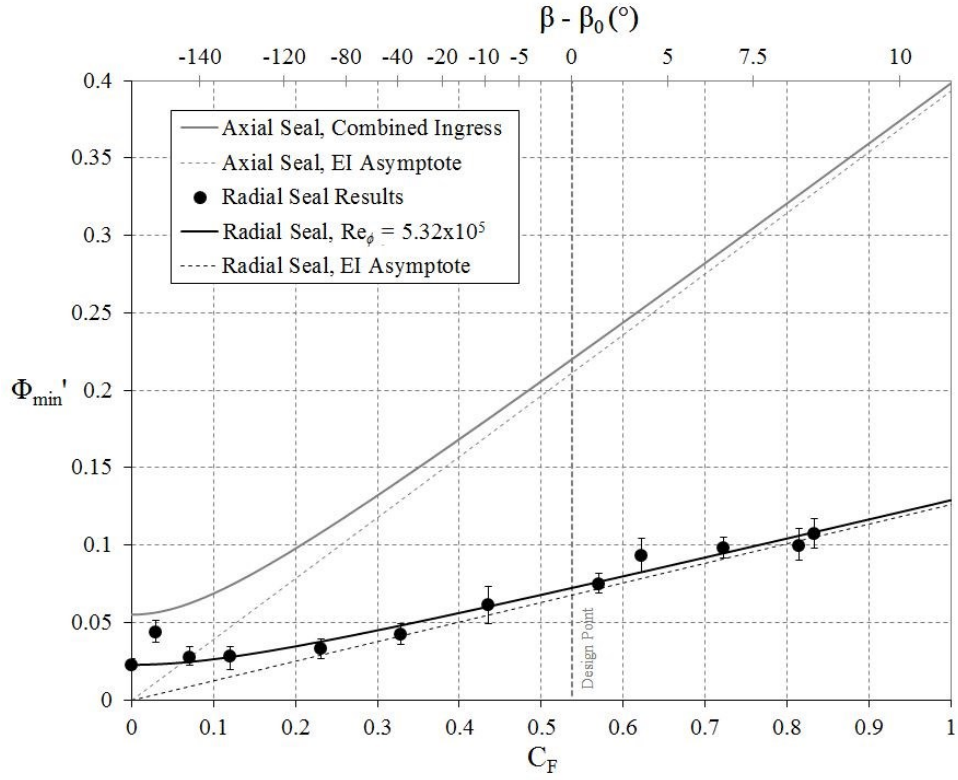


**Figure 15.** Variation of  $\Phi_{min}'$  with flow coefficient for radial-clearance seal

Solid symbols denote indirect values of  $\Phi_{min}'$  deduced from effectiveness curves

Solid lines are fitted CI curves; broken lines are EI asymptotes

Figure 15 shows the variation of  $\Phi_{min}'$  with flow coefficient for the radial-clearance seal. It can be seen that  $\Phi_{min}'$  is significantly smaller than for the axial-clearance seal, which is consistent with the results presented in Sangan et al.<sup>7,8</sup> for EI ingress in single seals. As for the radial-clearance seal, the ‘blade effect’ for the axial-clearance seal occurs only at very large deviation angles.

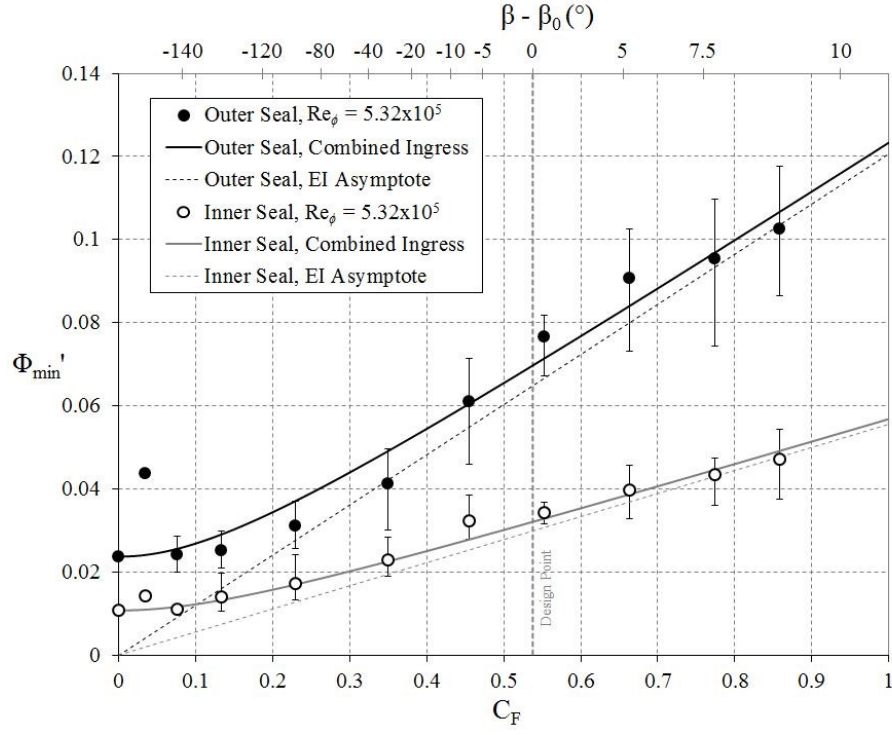


**Figure 16.** Variation of  $\Phi_{min}'$  with flow coefficient deduced from effectiveness curves for double seal

Solid and open symbols denote outer and inner seal respectively

Solid lines are fitted CI curves; broken lines are EI asymptotes

Figure 16 shows the variation of  $\Phi_{min}'$  with flow coefficient for the double seal. The results for the outer (radial-clearance) seal are similar to those shown above for the single radial-clearance seal, and the values of  $\Phi_{min}'$  for the inner seal are significantly smaller than for the outer one. Again this is consistent with results presented in Sangan et al.<sup>9</sup> for EI ingress in double seals.

The sharp increase in  $\Phi_{min}'$  at small  $C_F$  occurs at similar deviation angles to that found for all the seals tested. This suggests that the ‘blade effect’ is insensitive to seal geometry.

Parameter	Axial-Clearance Seal	Radial-Clearance Seal	Double Outer Seal	Double Inner Seal
$k_c$	115	70.4	58.3	60.3
$\Phi_{min,RI}'$	0.055	0.0226	0.0237	0.0107
$C_{d,e,El}'$	0.357	0.115	0.109	0.0503

**Table 2.** Parameters for CI fit for four seals tested

The results presented here were obtained for incompressible flow in a rig with symmetrical blades and over a  $C_F$  range much larger than the normal operating range of engines. It was shown above that the effect of blades is complicated and depends on the geometry and relative location of the vanes, blades and seal: in some studies, the blades had a favourable effect on ingress; in others, the effect was adverse. Except under extreme conditions, the current results showed no significant effect of the blades for any of the seals tested. Although the ‘blade effect’, or systematic departure of the measured values of  $\Phi_{min}'$  from the CI curves, only occurred here at extremely low values of  $C_F$ , it would be unsafe to conclude that this effect could not occur inside the operating range of a real turbine. (The fact that the measurements were made for incompressible flow is considered to be of secondary importance: extrapolation of effectiveness data from incompressible to compressible flow is discussed in Teuber et al.<sup>20</sup>)

It might seem surprising that the measured values of  $\Delta C_p$  provided no evidence of the ‘blade effect’: even at the smallest values of  $C_F$  measured, the variation of  $\Delta C_p^{1/2}$  with  $C_F$  remained linear. However, it has been shown computationally (see Zhou et al.<sup>6</sup>) that ingress is controlled by the magnitude of  $\Delta C_p$  near the seal clearance: presumably the measurements made on the vane platform and on the outer surface of the annulus were insensitive to the effects near the seal itself. As it is impracticable to measure  $\Delta C_p$  near the seal clearance, only CFD is likely to provide further information at this point.

## Conclusions

This paper presents off-design results for both over-speed, where the (symmetrical) blades rotate faster than at the design point, and under-speed conditions. The design flow coefficient was  $C_F = 0.538$ , and tests were conducted for  $0 < C_F < 0.9$ , which is a larger range than the operating range of engines. The ‘deviation angle’ between the flow over the blades and vanes, which increases as  $C_F$  decreases, varied between zero, at the design point, to 146 degrees at  $C_F = 0$ . Single and double seals were tested for rotational Reynolds numbers were in the range  $5.32 < Re_\phi/10^5 < 9.68$ , and the flow was incompressible. The sealing effectiveness,  $\varepsilon$ , was determined using concentration measurements with CO<sub>2</sub> tracer gas, and pressure measurements were made using a Scanivalve system.

For both rotationally-induced (RI) and externally-induced (EI) ingress, the Bath effectiveness equations were used to correlate the variation of  $\varepsilon$ , the sealing effectiveness, with  $\Phi_0$ , the nondimensional sealing flow parameter. The effectiveness equations were also used to determine  $\Phi_{min}'$ , the value of  $\Phi_0$  at  $\varepsilon = 0.95$ , and the combined ingress (CI) equation was used to correlate the variation of  $\Phi_{min}'$  with  $C_F$  and to determine the EI asymptote for each of the seals.

The principal conclusions are listed below.

- The pressure measurements showed that  $\Delta C_p^{1/2}$  (where  $\Delta C_p$  is the nondimensional peak-to-trough pressure difference in the annulus) was proportional to  $C_F$ . This proportionality occurred even at low values of  $C_F$ , where the deviation angle between the blades and vanes was very large ( $> 130^\circ$ ).
- For  $C_F > 0.1$ , and for all the seals tested, the CI equation was in mainly good agreement with the variation of  $\Phi_{min}'$  determined from the effectiveness curves; this implies that for a wide variation of  $C_F$  either side of the design point, the blade-deviation angle did not influence the degree of ingress.

- For  $C_F < 0.1$  and deviation angles  $> 130^\circ$ , there was a sharp increase in  $\Phi_{min}'$ ; this is believed to be a ‘blade effect’ caused by separation of the flow over the blades.
- The difference between the CI correlations and the EI asymptotes increased as  $C_F$  decreased, and there was even a small but significant difference at the design point of  $C_F = 0.538$ .

It should be noted that these conclusions were drawn from data obtained in an experimental rig, with symmetrical blades and no fillet radii, operating over a  $C_F$  range much larger than that experienced in engines. The ‘blade effect’, which only occurred in the rig for  $C_F < 0.1$ , might occur at larger values of  $C_F$  in the operating range of a real turbine.

In principle, and within the limits of dimensional similitude, the results presented here should apply to a geometrically-similar engine operating at the same fluid-dynamic conditions. It is shown for a large range of operating conditions,  $\Phi_{min}'$  is proportional to  $\Delta C_p^{1/2}$ , and it is tentatively suggested that this relationship could be used to extrapolate the results from an experimental rig to an engine.

## **Funding**

The research described here is part of a program funded by the UK Engineering and Physical Sciences Research Council.

## **Acknowledgement**

This article was originally presented as ASME Paper GT2013-94147<sup>22</sup> at the ASME International Gas Turbine and Aeroengine Technical Congress, Exposition and Users Symposium, June 3-7, 2013, in San

Antonio, USA. We thank the ASME for permission to publish this paper in the Proceedings of the Institution of Mechanical Engineers.

## References

1. Owen, J. M., 2011, "Prediction of Ingestion Through Turbine Rim Seals—Part I: Rotationally Induced Ingress," ASME J. Turbomach., 133, p. 031005. Formerly AMSE Paper No. GT2009-59121
2. Owen, J. M., 2011, "Prediction of Ingestion Through Turbine Rim Seals—Part II: Externally Induced and Combined Ingress," ASME J. Turbomach., 133, p. 031006. Formerly AMSE Paper No. GT2009-59122
3. Owen, J. M., Zhou, K., Pountney, O. J., Wilson, M., and Lock, G. D., 2012, "Prediction of Ingress Through Turbine Rim Seals. Part 1: Externally-Induced Ingress," ASME J. Turbomach., 134, p.031012. Formerly AMSE Paper No. GT2010-23346.
4. Owen, J. M., Pountney, O. J., and Lock, G. D., 2012, "Prediction of Ingress Through Turbine Rim Seals. Part 2: Combined Ingress," ASME J. Turbomach., 134, p.031013. Formerly AMSE Paper No. GT2010-23349.
5. Zhou, K., Wood, S. N., and Owen, J. M., 2013, "Statistical and Theoretical Models of Ingestion Through Turbine Rim Seals," ASME J. Turbomach., 135, p.021014. Formerly AMSE Paper No. GT2011-45139.
6. Zhou, K., Wilson, M., Owen, J. M., and Lock, G. D., "Computation of ingestion through gas turbine rim seals," Proc. IMechE Part G: J. Aerospace Engineering, 2013, 227, 1101-1113. Formerly AMSE Paper No. GT2011-45314.



7. Sangan, C. M., Pountney, O. J., Zhou, K., Wilson, M., Owen, J. M., and Lock, G. D., 2013, "Experimental Measurements of Ingestion Through Turbine Rim Seals. Part 1: Externally-Induced Ingress," ASME J. Turbomach., 135, p.021012. Formerly AMSE Paper No. GT2011-45310.
8. Sangan, C. M., Pountney, O. J., Zhou, K., Wilson, M., Owen, J. M., and Lock, G. D., 2013, "Experimental Measurements of Ingestion Through Turbine Rim Seals. Part 2: Rotationally-Induced Ingress," ASME J. Turbomach., 135, p.021013. Formerly AMSE Paper No. GT2011-45313.
9. Sangan, C. M., Pountney, O. J., Scobie, J.A., Wilson, M., Owen, J. M., and Lock, G. D., 2013, "Experimental Measurements of Ingestion Through Turbine Rim Seals. Part 3: Single and Double Seals," ASME J. Turbomach., 135, p.051011. Formerly AMSE Paper No. GT2012-68493.
10. Phadke, U.P., Owen, J.M., 1988, "Aerodynamic Aspects of the Sealing of Gas-Turbine Rotor-Stator Systems, Part 2: The Performance of Simple Seals in a Quasi-Axisymmetric External Flow", Int. J. Heat Fluid Flow, 9, pp. 106-112
11. Phadke, U. P., Owen, J. M., 1988, "Aerodynamic Aspects of the Sealing of Gas-Turbine Rotor-Stator Systems, Part 3: The Effect of Nonaxisymmetric External Flow on Seal Performance," Int. J. Heat Fluid Flow, 9, pp. 113–117.
12. Khilnani, V. I. and Bhavnani, S. H., 2001, "Sealing of gas turbine disk cavities operating in the presence of mainstream external flow," Exp. Thermal Fluid Sci. 25(3-4): pp. 163-173.
13. Green, T., and Turner, A. B., 1994, "Ingestion into the Upstream Wheelspace of an Axial Turbine Stage," ASME J. Turbomach, 116(2), pp. 327-332. Formerly AMSE Paper No. 92-GT-303.
14. Hills, N. J., Chew, J. W., and Turner, A. B., 2002, "Computational and Mathematical Modeling of Turbine Rim Seal Ingestion," ASME J. Turbomach., 124, pp. 306-315. Formerly AMSE Paper No. 2001-GT-0204.

15. Bohn, D., Rudzinsky, B., Surken, N., and Gartner, W., 2000, "Experimental and Numerical Investigation of the Influence of Rotor Blades on Hot Gas Ingestion Into the Upstream Cavity of an Axial Turbine Stage," ASME Paper 2000-GT-284.
16. Bohn, D. E., Decker, A., Ma, H. and Wolff, M., 2003, "Influence of Sealing Air Mass Flow on the Velocity Distribution in and Inside the Rim of the Upstream Cavity of a 1.5-Stage Turbine," ASME Paper No. GT2003-38459.
17. Gentilhomme, O., Hills, N. J., Turner, A. B., and Chew, J.W., 2002, "Measurement and Analysis of Ingestion Through a Rim Seal," ASME J. Turbomach., 125. pp. 505-512. Formerly AMSE Paper No. GT2002-30481.
18. O'Mahoney, T. S. D., Hills, N. J., Chew, J.W., and Scanlon, T., "Large-Eddy simulation of rim seal ingestion," Proc. IMechE Part C: J. Engineering and Science, 2011, 225, 2881-2891. Formerly ASME Paper No. GT2010-22962
19. Owen, J. M., and Rogers, R. H., 1989, Flow and Heat Transfer in Rotating-Disc Systems, Volume 1—Rotor Stator Systems, Research Studies Press Ltd., Taunton, UK.
20. Teuber, R., Wilson, M., Lock, G. D., Owen, J. M., Li, S., and Maltson, J. D., "Computational extrapolation of turbine sealing effectiveness from test rig to engine conditions," Proc. IMechE Part A: J. Power and Energy, 2013, 227, 167-178. Formerly AMSE Paper No. GT2012-68490.
21. Bohn, D., and Wolff, M., 2003, "Improved Formulation to Determine Minimum Sealing Flow— $C_{w, min}$ —for Different Sealing Configuration," ASME Paper No. GT2003-38465.
22. Scobie, J. A., Sangan, C. M., Teuber, R., Pountney, O. J., Owen, J. M., Wilson, M., and Lock, G. D., 2013, "Experimental Measurements of Ingestion Through Turbine Rim Seals. Part 4: Off-Design Conditions," AMSE Paper No. GT2013-94147.

## Appendix 1

### Notation

$b$	radius of seal
$c$	concentration
$C_{d,e} C_{d,i}$	discharge coefficients for egress, ingress
$C_F$	flow coefficient [ $= W / \Omega b$ ]
$C_p$	pressure coefficient [ $= (p - \bar{p}) / (1/2 \rho \Omega^2 b^2)$ ]
$C_w$	non-dimensional flow rate [ $= \dot{m} / \mu b$ ]
$C_{w,0}$	non-dimensional sealing flow rate
$C_{w,min}$	minimum value of $C_{w,0}$ to prevent ingress
$C_{\beta 1}$	modified internal swirl ratio [ $= \beta_1^2 / (1 - r_1^2 / r_2^2)$ ]
$G_c$	seal-clearance ratio [ $= s_c / b$ ]
$h_{buffer}$	depth of buffer cavity
$K, k_a, k_c$	empirical constants
$\dot{m}$	mass flow rate
$p$	absolute static pressure
$r$	radius
$Re_w$	axial Reynolds number in annulus [ $= \rho W b / \mu$ ]
$Re_\phi$	rotational Reynolds number [ $= \rho \Omega b^2 / \mu$ ]
$s_c$	seal clearance
$s_{overlap}$	axial overlap of radial clearance seal
$U$	bulk-mean velocity through rim-seal clearance
$V_\phi$	tangential component of velocity
$W$	axial velocity in annulus

$\alpha$	vane exit angle
$\beta$	blade angle; swirl ratio in wheel-space [ $= V_\phi / \Omega r$ ]
$\beta - \beta_0$	deviation angle
$\Delta C_p$	non-dimensional pressure difference [ $= \Delta p / (1/2 \rho \Omega^2 b^2)$ ]
$\Delta p$	peak-to-trough pressure difference in annulus [ $= p_{max} - p_{min}$ ]
$\Gamma_c$	ratio of discharge coefficients [ $= C_{d,i} / C_{d,e}$ ]
$\Gamma_{\Delta p}$	ratio of driving force for EI and RI ingress [ $= \Delta C_p / C_{\beta 1}$ ]
$\varepsilon$	sealing effectiveness [ $= C_{w,0} / C_{w,e} = \Phi_0 / \Phi_e$ ]
$\varepsilon_c$	concentration effectiveness [ $= (c_s - c_a) / (c_o - c_a)$ ]
$\Phi$	non-dimensional sealing parameter [ $= C_w / 2\pi G_c Re_\phi$ ]
$\Phi_i$	value of $\Phi$ when $C_w = C_{w,i}$
$\Phi_{min}$	value of $\Phi$ when $C_w = C_{w,min}$
$\Phi_{min}'$	value of $\Phi_0$ when $\varepsilon = 0.95$
$\Phi_0$	value of $\Phi$ when $C_w = C_{w,0}$
$\theta$	angular coordinate, non-dimensional vane pitch
$\lambda_T$	turbulent flow parameter [ $= C_{w,0} Re_\phi^{-0.8}$ ]
$\mu$	dynamic viscosity
$\rho$	density
$\Omega$	angular velocity of rotating disc

### *Subscripts*

$a$	annulus
$CI$	combined ingress
$e$	egress

<i>EI</i>	externally-induced ingress
<i>i</i>	ingress
<i>max</i>	maximum
<i>min</i>	minimum
<i>RI</i>	rotationally-induced ingress
<i>s</i>	stator
<i>0</i>	superposed flow; design condition

## Appendix 2

### *Equations for orifice model*

Theoretical *orifice models* [1-9] have been developed at the University of Bath, and these models have had good success in correlating the sealing effectiveness of rim seals for CI, EI and RI ingress. The models treat the seal clearance as an orifice and use variations of Bernoulli's equation, including swirl terms, to relate the sealing flow rate to the pressure drop across the seal. Although the equations are derived for inviscid incompressible flow, discharge coefficients, analogous to those used for the standard orifice equations, are introduced to account for losses. In general, different discharge coefficients ( $C_{d,i}$  and  $C_{d,e}$ ) are needed for ingress and egress, and these have to be determined empirically.

The so-called *effectiveness equations* express  $\varepsilon$ , the sealing effectiveness, in terms of  $\Phi_0$ , the sealing parameter, which is defined as

$$\Phi_0 = \frac{C_{w,0}}{2\pi G_c Re_\phi} = \frac{U}{\Omega b} \quad (16)$$

where  $U$  is the bulk-mean velocity through the rim-seal clearance and the other symbols are defined in the Appendix 1.

*Externally-induced ingress.* The EI effectiveness equation when  $\Phi_0 \leq \Phi_{min,EI}$  is,

$$\frac{\Phi_0}{\Phi_{min,EI}} = \frac{\varepsilon}{[1 + \Gamma_c^{-2/3} (1 - \varepsilon)^{2/3}]^{3/2}} \quad (17)$$

where  $\Gamma_c$  is the ratio of the discharge coefficients for ingress and egress, and

$$\Phi_{min,EI} = \frac{2}{3} C_{d,e} \Delta C_p^{1/2} \quad (18)$$

where

$$\Delta C_p = \frac{\Delta p}{\frac{1}{2} \rho \Omega^2 b^2} \quad (19)$$

$\Delta p$  is the peak-to-trough circumferential pressure difference in the annulus, and  $C_{d,e}$  is the discharge coefficient for egress through the rim seal. When  $\Phi_0 > \Phi_{min,EI}$ ,  $\varepsilon = 1$ .

Some research workers<sup>11,21</sup> have used a  $K$  factor to rank the performance of rim seals. It can be shown that

$$K = \frac{\sqrt{2} \Phi_{min,EI}}{\Delta C_p^{1/2}} = \frac{2\sqrt{2}}{3} C_{d,e} \quad (20)$$

*Rotationally-induced ingress.* The RI effectiveness equation when  $\Phi_0 \leq \Phi_{min,RI}$ ,

$$\frac{\Phi_0}{\Phi_{min,RI}} = \frac{\varepsilon}{[1 + (1 - \varepsilon)^{1/2}][1 + \Gamma_c^{-2} (1 - \varepsilon)]^{1/2}} \quad (21)$$

where

$$\Phi_{\min,RI} = C_{d,e} C_{\beta 1}^{1/2} \quad (22)$$

and  $C_{\beta 1}$  is an empirical constant. When  $\Phi_0 > \Phi_{\min,RI}$ ,  $\varepsilon = 1$ .

*Combined ingress.* Equation (18) applies when the effect of rotation is negligible and equation (22) applies when  $\Delta C_p$  is negligible. These two equations provide the EI and RI asymptotes, and the combined ingress (CI) equation provides a transition between these limiting cases when the effects of both rotation and pressure asymmetry are significant. For the CI case

$$\frac{\Phi_{\min,CI}}{\Phi_{\min,RI}} = \frac{2}{3} \frac{C_{d,e,CI}}{C_{d,e,EI}} \frac{[1 + \Gamma_{\Delta p}]^{3/2} - 1}{\Gamma_{\Delta p}} \quad (23)$$

where

$$\Gamma_{\Delta p} = \frac{\Delta C_p}{C_{\beta 1}} \quad (24)$$

and, from equation (22),

$$C_{\beta 1} = \left[ \frac{\Phi_{\min,RI}}{C_{d,e,RI}} \right]^2 \quad (25)$$

For simplicity, it is assumed here that  $C_{d,e,CI} = C_{d,e,RI} = C_{d,e,EI}$ .

As shown in equation (13),

$$\Delta C_p^{1/2} = k_a C_F \quad (26)$$

where  $k_a$  is found from least-squares fit to the pressure data. It follows that

$$\Gamma_{\Delta p} = k_c C_F^2 \quad (27)$$

where

$$k_c = \left[ \frac{k_a C_{d,e,RI}}{\Phi_{\min,RI}} \right]^2 \quad (28)$$

Using equation (27), equation (16) becomes

$$\frac{\Phi_{\min,CI}}{\Phi_{\min,RI}} = \frac{2}{3} \frac{\left[ 1 + k_c C_F^2 \right]^{3/2} - 1}{k_c C_F^2} \quad (29)$$